Magneto-optic response of the metallic antiferromagnet Fe_2As to ultrafast temperature excursions

Kexin Yang,[1,2] Kisung Kang,[2,3] Zhu Diao,[2,4,5,*] Arun Ramanathan,[2,3] Manohar H. Karigerasi,[2,3] Daniel P. Shoemaker,[2,3]
André Schleife,[2,3,6,†] and David G. Cahill[1,2,3,‡]
[1]Department of Physics, University of Illinois at Urbana-Champaign, Urbana, Illinois 61801, USA
[2]Materials Research Laboratory, University of Illinois at Urbana-Champaign, Urbana, Illinois 61801, USA
[3]Materials Science and Engineering, University of Illinois at Urbana-Champaign, Urbana, Illinois 61801, USA
[4]Department of Physics, Stockholm University, SE-106 91 Stockholm, Sweden
[5]School of Information Technology, Halmstad University, P.O. Box 823, SE-301 18 Halmstad, Sweden
[6]National Center for Supercomputing Applications, University of Illinois at Urbana-Champaign, Urbana, Illinois 61801, USA

(Received 6 August 2019; revised manuscript received 22 October 2019; published 23 December 2019)

The linear magneto-optic Kerr effect (MOKE) is often used to probe magnetism of ferromagnetic materials, but MOKE cannot be applied to collinear antiferromagnets due to the cancellation of sublattice magnetization. Magneto-optic constants that are quadratic in magnetization, however, provide an approach for studying antiferromagnets on picosecond timescales. Here, we combine transient measurements of linear birefringence and optical reflectivity to study the optical response of Fe_2As to small ultrafast temperature excursions. We performed temperature-dependent pump-probe measurements on crystallographically isotropic (001) and anisotropic (010) faces of Fe_2As bulk crystals. We find that the largest optical signals arise from changes in the index of refraction along the z axis, perpendicular to the Néel vector. Both real and imaginary parts of the transient optical birefringence signal approximately follow the temperature dependence of the magnetic heat capacity, as expected if the changes in dielectric function are dominated by contributions of exchange interactions to the dielectric function.

DOI: 10.1103/PhysRevMaterials.3.124408

I. INTRODUCTION

Antiferromagnetic materials are under intense investigation as a new generation of spintronic materials because of their robustness to external magnetic fields and ultrafast dynamics, as it manifests itself, for instance, in a higher resonance frequency, compared with ferromagnets [1–5]. Characterization of the structure and dynamics of the magnetic order parameter is essential for spintronics research but is difficult to achieve in antiferromagnets (AFs). Magneto-optic effects are often a valuable tool for probing magnetic order; for example, much of what is known about the dynamics of ferromagnetic and ferrimagnetic materials comes from studies that make use of the linear magneto-optic Kerr effect (MOKE) [6,7]. Linear MOKE is also an essential tool for imaging the structure of magnetic domains [6,8]. For typical AFs, however, linear MOKE is absent. Application of linear MOKE in the study of AFs is mostly limited to AFs with weak ferromagnetism due to canted magnetic moments, e.g., in orthoferrites [9]. More recently, relatively large linear magneto-optic effects were observed in the *noncollinear* AF Mn_3Sn [10,11].

The structure and dynamics of the order parameter of AFs can be probed using interactions that are quadratic in the magnetization. For example, anisotropic magnetoresistance (AMR) depends on contributions to electronic relaxation times that are quadratic in magnetization; AMR is sensitive to the domain structure of AFs [12]. More recently, AMR was used to read the spin configuration of antiferromagnetic CuMnAs [13] and Mn_2Au [14]. At x-ray wavelengths, magnetic linear dichroism (XMLD) probes the anisotropy of charge distributions that are quadratic in magnetization [15].

Magnetic linear birefringence and magnetic linear dichroism refer to anisotropies in the optical frequency dielectric function that are generated by terms that are second-order in the magnetization. The dielectric function and the second-order terms of magnetization are both second rank tensors; therefore, the quadratic magneto-optic coefficients form a fourth-rank tensor. Since changes in optical phase accumulate over the optical path length, weak magneto-optic effects are easier to study in transmission through optically transparent materials than in reflection from the surface of opaque materials [16].

For transparent materials, experimentalists usually study magnetic linear birefringence because polarimetry [16] can sensitively detect differences between the optical path lengths for light polarized along orthogonal directions of the sample. In cubic crystals, this experimental design can isolate the anisotropic contributions to the magneto-optic coefficients, i.e., contributions to the magneto-optic tensor that depend on the orientation of the Néel vector. Isotropic contributions to the dielectric function—i.e., contributions to the magneto-optic tensor that are independent of the orientation of the Néel vector—can also be significant and lead to effects that are often referred to as magneto-refraction [17]. The

---

[*] Present address: Department of Physics, Florida A&M University, Tallahassee, Florida 32307 USA.

[†] schleife@illinois.edu

[‡] d-cahill@illinois.edu

orientation of the magnetization of a material with a net magnetic moment can often be manipulated by an external magnetic field; control of the orientation of the Néel vector of collinear AFs is more difficult. Therefore, the various elements of the fourth-rank tensor are more accessible to experiments on ferromagnets and weak ferromagnets than AFs.

In 2017, Saidl *et al.* [18] reported their studies of the time-resolved magneto-optic response of AF CuMnAs to a large temperature excursion, $\Delta T \sim 100$ K. CuMnAs films were grown epitaxially on GaP(001) substrates with the z axis, the hard magnetic axis of CuMnAs, parallel to the surface normal. The magnetic structure of tetragonal CuMnAs has two degenerate magnetic domains with perpendicular Néel vectors in the x-y plane. For a 10-nm-thick CuMnAs layer, the authors observed a rotation of the polarization of the optical probe beam that is consistent with magnetic linear birefringence. They observed that changes in the angle of polarization followed $\Delta\theta \propto \sin 2\alpha$, where α is the angle between the Néel vector and the polarization of the probe beam.

In our work, we studied transient changes in the optical frequency dielectric function of the metallic AF Fe_2As, produced by a small temperature excursion, $\Delta T \approx 3$ K. We acquired data for changes in birefringence and reflectivity using techniques that we refer to as time-domain thermo-birefringence (TDTB) and time-domain thermo-reflectance (TDTR). TDTB and TDTR signals are acquired by using a pump-probe apparatus based on a high-repetition-rate Ti:sapphire laser oscillator operating at a wavelength near 785 nm. We also measured the total heat capacity of Fe_2As as a function of temperature and isolated the magnetic contribution to the measured heat capacity by subtracting the electronic and phonon heat capacities calculated by density-functional theory (DFT).

Fe_2As crystallizes in the Cu_2Sb tetragonal crystal structure as shown in Fig. 1(a) [19]. Early neutron diffraction studies showed that the spin magnetic moments of Fe_2As lie in x-y plane [19]. Subsequent studies by torque magnetometry [20] at liquid nitrogen temperature showed that the vector has two degenerate orientations in the x and y directions. The magnetic point group of this magnetic structure is $mmm1'$ [21]. The equivalence of the x axis and y axis was supported by the magnetic-field dependence of neutron diffraction at room temperature and close to the Néel temperature [22]. This type of magnetic structure is typically referred to as a tetragonal "easy-plane" antiferromagnet [16]. The term easy-plane refers to the fact that the lowest energy orientations of the Néel vector lie in the x-y plane. The term easy-plane does not exclude the possibility of small differences in energy for different orientations of the Néel vector within the x-y plane.

In the absence of magnetic order, the dielectric tensor of a tetragonal crystal is isotropic in the x-y plane. However, if the Néel vectors have a preferred direction in the x-y plane, the dielectric function is anisotropic on length scales smaller or comparable to the characteristic size of the magnetic domains. We expect that the Néel vector of different magnetic domains are randomly oriented along the x and y directions and that our laser beam size is large compared with the domain size. Therefore, the dielectric function we measure in the x-y plane is isotropic. We indeed do not observe a significant TDTB signal for the (001) surface of Fe_2As. However, on the crystallographically anisotropic (010) surface of the tetragonal crystal, we observed a strong TDTB signal for light polarized at an angle of 45° between the x and z axis of the crystal. We gain complementary insight by measuring the TDTR signals for light polarized along the x and z axes.

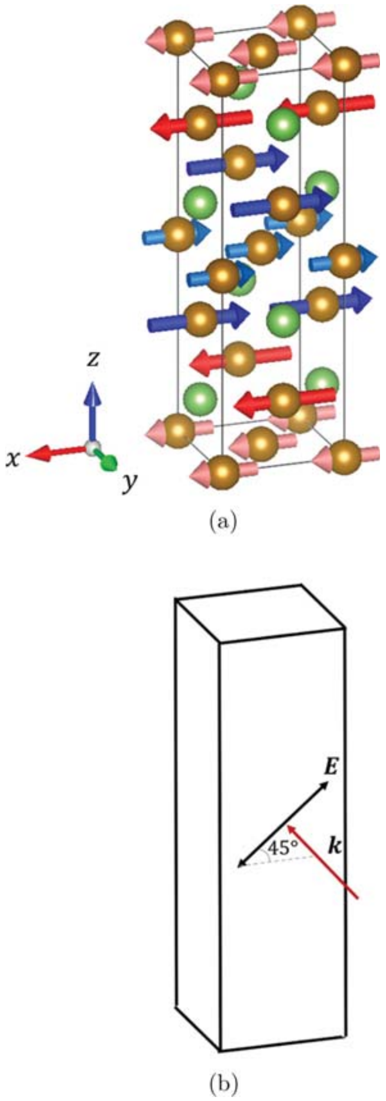

FIG. 1. (a) Tetragonal magnetic unit cell of Fe_2As. Arsenic atoms are depicted as green spheres; Fe as brown spheres. Arrows denote the local magnetic moment of the Fe atoms. Fe atoms labeled with the same color arrows (blue or pink) are crystallographically equivalent. The Cartesian coordinates x, y, z are aligned along the crystallographic a, b, c axes. (b) Experimental geometry for time-domain thermo-birefringence (TDTB) and time-domain thermoreflectance (TDTR) experiments with the probe beam normal to the (010) face of the Fe_2As crystal. In TDTR measurements, the polarization of the probe is along x or z. In TDTB measurements, the polarization of the electric field E of the probe is at an angle of 45° from the x axis.

Often, magnetic linear birefringence of magnetic materials is attributed to the Voigt effect. The Voigt effect refers to anisotropic contributions to the dielectric tensor that are *parallel* to the magnetization [16,23]. However, our data imply that the most significant change in the dielectric function is perpendicular to the Néel vector: $\Delta\varepsilon_{33} \gg \Delta\varepsilon_{11}$. Furthermore, the dependence of the TDTB signal on the sample temperature closely resembles the magnetic heat capacity, suggesting a proportionality between the temperature dependence of the exchange energy and the temperature dependence of the z element of the dielectric function ε_{33}.

Our experiments also provide insight into the ultrafast magnetization dynamics of Fe_2As. By comparing changes in the magneto-optic response at short and long timescales, we also evaluate the importance of magnetostriction to magnetic linear birefringence in this material.

II. EXPERIMENTS

A. Experimental details

Single crystals of Fe_2As were synthesized from the melt. Stoichiometric amounts of elemental Fe and As (99.8% and 99.999%, Alfa Aesar) were ground inside an argon-filled glove box in an agate mortar and pestle. The powder mixture was loaded in a 6-mm-diameter fused silica tube and sealed under vacuum. The tube was heated at 5 °C/min to 700 °C and held for 24 h, then 1000 °C for 2 h with a 5 °C/min ramp rate. The tube was cooled to 900 °C in 20 h, then cooled at 5 °C/min to obtain shiny gray crystals of Fe_2As. The phase purity of the sample was confirmed by using powder x-ray diffraction on a Bruker D8 diffractometer with a Mo Kα source and LYNXEYE XE detector in the transmission geometry. Rietveld refinements were performed by using TOPAS 5. The lattice constants at room temperature are $a = 3.63$ Å, $c = 5.98$ Å.

Before optical measurements, the Fe_2As sample was polished along the (001) and (010) orientation with an Allied Multiprep automatic polisher with diamond lapping films down to 0.3 μm. The orientation was observed via x-ray diffraction pole figures. The miscut of the surfaces is within 10°. After polishing, the sample was ion-milled for 5 min by using a broad-beam Ar-ion source operating at 250 V and 60 mA.

TDTB and TDTR measurements were done with a pump-probe system that employs a Ti:sapphire laser with a 80 MHz repetition rate and 783 nm center wavelength. The spectral linewidth of the output of the laser is 12 nm. We use sharp-edge optical filters to spectrally separate the pump and probe [24]. The full width at half maximum of the pump-probe correlation is 1.1 ps. The pump beam is modulated at 10.8 MHz and the probe beam is modulated at 200 Hz. A half-wave plate was placed in the probe beam path to orient the polarization of probe beam. For TDTB experiments, the transient change in the polarization or ellipticity of the probe was captured by a balanced photodetector; in TDTR experiments, the transient reflection was measured by a single Si photodetector [25]. The $1/e$ laser spot size of both the focused pump and probe beams is 5.5 μm. The fluence of the pump is 0.22 J/m^2, which created a steady-state heating of ≈13 K and transient heating of ≈3 K on the sample surface. The zero of time delay was determined by using a GaP two-photon photodetector. For temperature-dependent measurements, the sample was mounted on a temperature-controlled microscope stage in a vacuum of ~1 mTorr.

We performed first-principles calculations using density-functional theory (DFT) as implemented in the Vienna *ab initio* Simulation Package [26–28] (VASP). The generalized-gradient approximation (GGA) formulated by Perdew, Burke, and Ernzerhof [29] (PBE) is used to describe exchange and correlation. The projector-augmented wave [30] (PAW) scheme is used to describe the electron-ion interaction. To sample the Brillouin zone, a 15 × 15 × 5 Monkhorst-Pack (MP) [31] **k**-point grid is used and the Kohn-Sham states are expanded into plane waves up to a cutoff energy of 600 eV. Total energies are converged to self-consistence within 10^{-6} eV. Noncollinear magnetism and spin-orbit coupling are included and the magnetic unit cell of Fe_2As is used to compute relaxed atomic geometries, electronic structure, and optical properties. Phonon dispersion is computed by using the finite displacement method as implemented in VASP and extracted by using the phonopy package [32]. After convergence test, a 3 × 3 × 2 supercell and 4 × 4 × 4 MP **k**-point grid is used. For the phonon calculations, noncollinear magnetism and spin-orbit coupling is included.

B. Optical and thermal properties

First, we discuss measurements of refractive index, electrical conductivities, heat capacity, and thermal conductivities of Fe_2As. We use the refractive index to describe the optical properties of the material and to make connections between thermo-reflectance and thermo-birefringence data. We measure the total heat capacity and use density-functional theory to calculate the electronic and phonon contributions to the total heat capacity. We attribute the heat capacity that is unaccounted for by electrons and phonons to the magnetic heat capacity and compare the magnetic heat capacity to the temperature-dependent TDTB data. From the heat capacity and thermal conductivity, we model the time-evolution of the temperature excursion created by the pump optical pulse. Finally, the combination of the measured electrical conductivity and the Wiedemann-Franz law allows us to separate the electronic and lattice contributions to the total thermal conductivity.

First-principles density-functional theory (DFT) calculations give the ground-state lattice parameters as $a = 3.624$ Å and $c = 5.860$ Å, within 2% of powder x-ray diffraction measurements at room temperature, $a = 3.63$ Å and $c = 5.98$ Å. The magnetic unit cell used in the calculation is twice as long in the z direction. The Néel vector in ground-state DFT calculations is oriented along the x direction of the lattice. We confirmed the easy-plane magnetic structure by measuring the temperature-dependent magnetic susceptibilities along the x and z crystallographic directions with a vibrating sample magnetometer.

We measured an effective isotropic refractive index of Fe_2As by spectroscopic ellipsometry of the (001) and (010) faces of the crystal. Immediately prior to the ellipsometry measurements, which take place under ambient conditions, we removed surface oxides and contaminants using argon-ion beam milling. The effective isotropic refraction index is

$n = 2.9 + i3.3$ at a wavelength of $\lambda = 780$ nm. The optical reflectance calculated from this index of refraction is 0.56. The measured optical reflectance for both the (001) and (010) surfaces of the crystal at normal incidence and $\lambda = 780$ nm is 0.50. The optical absorption depth, $\lambda/(4\pi k)$, is 19 nm. The refractive index computed using DFT, for light polarized along the x, y, and z axis of the crystal is $n_i = \sqrt{\varepsilon_{ii}} = 4.295 + i3.496$, $4.300 + i3.501$, and $3.381 + i4.039$ at 0 K, with a reflectance of 0.573, 0.574, and 0.619, respectively.

The electrical resistivity of a polycrystalline sample of Fe_2As was reported previously as $\rho \approx 220$ $\mu\Omega$cm at $T = 300$ K [33]. The electrical resistivity has a shallow maximum near room temperature and decreases to $\approx$125 $\mu\Omega$cm at $T = 1$ K. The electrical resistivity of our samples near room temperature is $\rho = 240\,\mu\Omega$cm; the residual resistivity ratio (RRR), the resistivity at 300 K divided by the resistivity at 7 K, is 1.7. We attribute the small RRR to Fe vacancies. The stoichiometry of Fe_2As was evaluated by using Rutherford backscattering spectrometry and Rietveld refinements to synchrotron x-ray and neutron diffraction data (see Supplemental Material [34]). These measurements converge on a Fe deficiency of 0.05 to 0.08 out of 2. This value also agrees with the nominal Fe:As ratio used during synthesis (1.95 : 1). (Nominally 2.00 : 1 samples exhibit metallic Fe impurities.)

We measured the total heat capacity of a 35.5 mg sample of Fe_2As with a Quantum Design Physical Property Measurement System (PPMS), see Fig. 2(a). As we discuss below, we expect that the temperature derivative of the magnetic contribution to the dielectric function will be proportional to the magnetic heat capacity. The total heat capacity includes, however, contributions from electrons, phonons, and magnetic excitations. We isolate the magnetic contribution C_m to the measurement of the total heat capacity C_{tot} by subtracting the electron and phonon heat capacities calculated with density-functional theory (DFT): $C_m = C_{\text{tot}} - C_e - C_{\text{ph}}$. We computed the electronic density of states using Mermin DFT [35] and finite electronic temperatures between 0 and 400 K; see Fig. 3(a) for 300 K. From these data we calculate the electronic heat capacity C_e and electronic specific heat $\gamma = 7.41\ \text{mJ}\,\text{K}^{-2}\,\text{mol}^{-1}$. The phonon heat capacity C_{ph} is calculated from the phonon density of states (DOS) of the ground-state crystal structure and magnetic order; see Fig. 3(b). The Debye temperature derived from the calculated phonon DOS is 286 K. Zocco *et al.* [33] reported a Debye temperature of 296 K for Fe_2As from a linear fit of their data to C/T versus T^2.

Because the lattice heat capacity dominates the total heat capacity except at low temperatures, $T < 15$ K, small errors in the measurement of the total heat capacity, or small errors in the calculation of the phonon heat capacity, produce large uncertainties in the magnetic heat capacity. We do not yet understand the origin of the small peak in the heat-capacity data near 110 K.

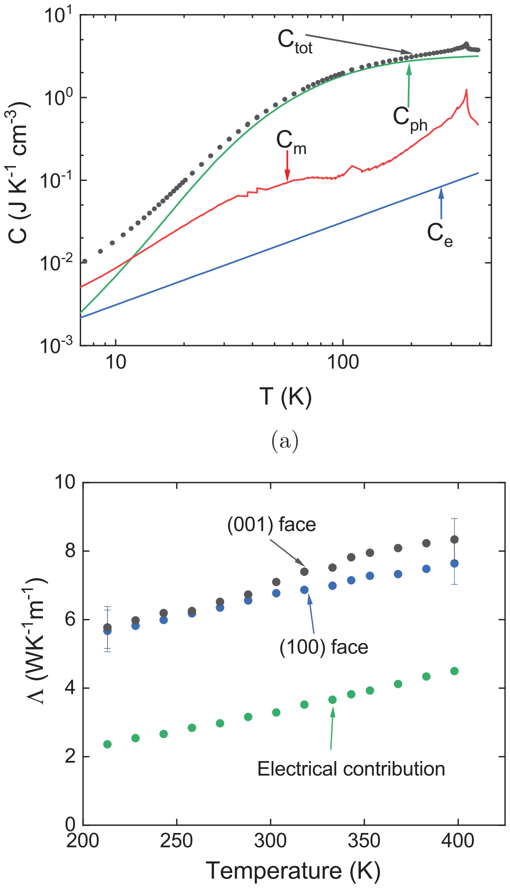

(a)

(b)

FIG. 2. Heat capacity and thermal conductivity of Fe_2As. (a) The measured total heat capacity C_{tot} of Fe_2As and contributions to C_{tot} from excitations of electrons (e), phonons (ph), and magnons (m). The electronic and phonon contributions are calculated by density-functional theory (DFT). The magnon contribution is derived by subtracting the calculated phonon and electronic contributions from C_{tot}. (b) The thermal conductivity in the direction normal to the (001) face (black circles) and (100) face (blue circles) shows a small anisotropy. The electrical contribution to the thermal conductivity (green circles) is calculated from the Wiedemann-Franz law and measurements of the electrical conductivity.

We also measured the thermal conductivity of Fe_2As normal to the (001) and (010) faces of the crystal using conventional TDTR measurements and modeling [36] as shown in Fig. 2(b). An 80-nm-thick Al film was sputtered on the sample to serve as the optical transducer in the thermal-conductivity measurement. The electrical contribution to the thermal conductivity was estimated by using the combination of the Wiedemann-Franz law and the measured electrical resistivity. The thermal conductivity shows a small anisotropy at $T > 300$ K [see Fig. 2(b)]. Contributions to the thermal conductivity from phonons and electronic excitations are comparable. The phonon contribution, i.e., the difference between the measurement and the electronic contribution, is approximately 3.6 W K^{-1} m^{-1} and independent of temperature.

C. Time-domain thermo-birefringence and time-domain thermoreflectance

Time-domain thermo-birefringence (TDTB) and time-domain thermoreflectance (TDTR) probe transient changes in the optical frequency dielectric function of Fe_2As induced by excitation of the sample by the pump beam. We use TDTR to measure changes in the diagonal elements of the

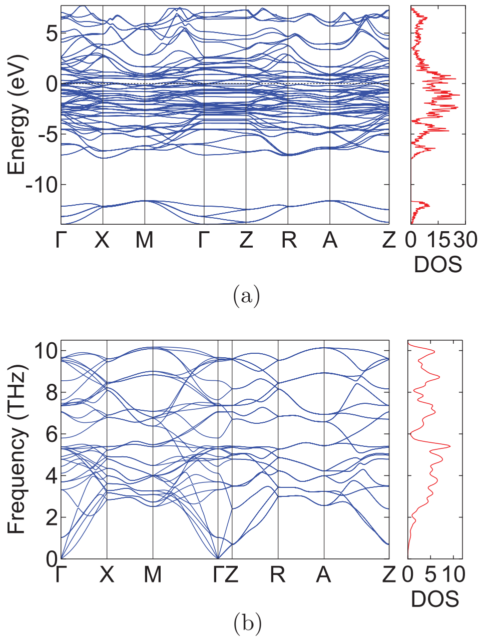

(a)

(b)

FIG. 3. (a) Calculated electronic band structure and electronic density of states (DOS) of Fe_2As. The electronic band structure includes spin-orbit coupling effects through a noncollinear magnetism calculation. (b) Calculated phonon dispersion and phonon DOS of Fe_2As. For panel (a), the units of the electronic DOS are the number of states per magnetic unit cell per eV; for panel (b), the units of the phonon DOS are the number of states per magnetic unit cell per THz.

dielectric tensor by fixing the probe polarization along various crystallographic directions and measuring transient changes in the *intensity* of the reflected probe pulse. We use TDTB to measure changes in differences between diagonal elements of the dielectric tensor through transient changes in the *polarization* of the reflected probe pulse. For both TDTB and TDTR, the strongest signals we have observed are for pump and probe beams at normal incidence on the crystallographically anisotropic (010) surface of Fe_2As.

The dielectric function tensor of Fe_2As is diagonal in the coordinate system defined by the crystal axes; off-diagonal elements of dielectric tensor are zero [21] for the $mmm1'$ magnetic point group. In our experiments, heating by the pump optical pulse creates changes in the thermal distribution of magnetic excitations. In other words, in our experiments, the excitations created by the pump are incoherent. The situation is different in pump-probe experiments that create coherent excitations of magnons. For example, in a recent study of the cubic collinear antiferromagnet $KNiF_3$ [37], both diagonal and off-diagonal elements of the dielectric tensor contribute to magnetic linear birefringence because the circularly polarized pump pulse excites a coherent magnon that breaks the underlying magnetic symmetry.

The TDTB measurement geometry is shown in Fig. 1(b) and the measurement results for the Fe_2As (010) face are shown in Fig. 4. In the discussion that follows, the symbol Δ indicates a transient quantity. To measure transient changes in the real part of the polarization rotation, $\mathrm{Re}[\Delta\Theta] = \Delta\theta$, we null the balanced detector with a half-wave plate. (This half-wave plate is positioned immediately before the Wollaston prism that splits the orthogonal polarizations into two paths that are focused onto the two photodiodes of the balanced detector [25].) To measure transient changes in the imaginary part of the rotation, i.e., the ellipticity $\mathrm{Im}[\Delta\Theta] = \Delta\kappa$, we null the balanced detector with a quarter-wave plate. The polarization of the probe beam is in the x-z plane and 45° from the x axis. Corresponding TDTR data for the (010) face of Fe_2As is shown for the two orthogonal polarizations in Fig. 5.

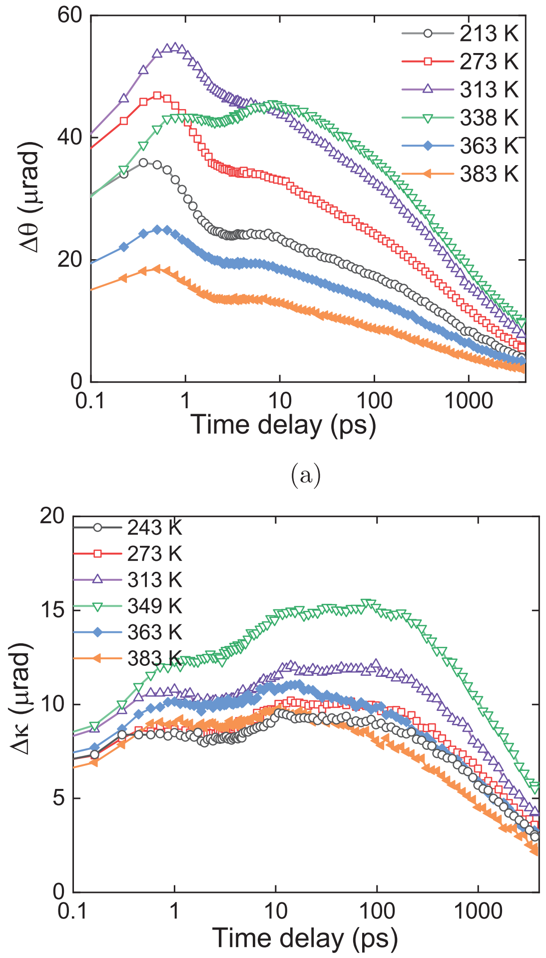

(a)

(b)

FIG. 4. (a) The real part of the time-domain thermo-birefringence (TDTB) signal measured on the (010) face of Fe_2As; and (b) the imaginary part of the TDTB signal. The temperature in the legend is the temperature of the sample stage; the spatially averaged temperature of the area of the sample that is measured in the TDTB experiment is the sum of the stage temperature and the steady-state heating of 13 K. When stage temperature is at 338 K, the temperature of the measured region of the sample is close to $T_N = 350$ K. Empty symbols denote data acquired at $T < T_N$; filled circles are data for $T > T_N$. We attribute the slower response at $T \approx T_N$ to the peak in the magnetic heat capacity at T_N.

Optical reflectance R is the ratio of the intensity of the reflected electrical field to the intensity of the incident electric field: $R_z = |r_z|^2$ and $R_x = |r_x|^2$ where r_z and r_x are the Fresnel

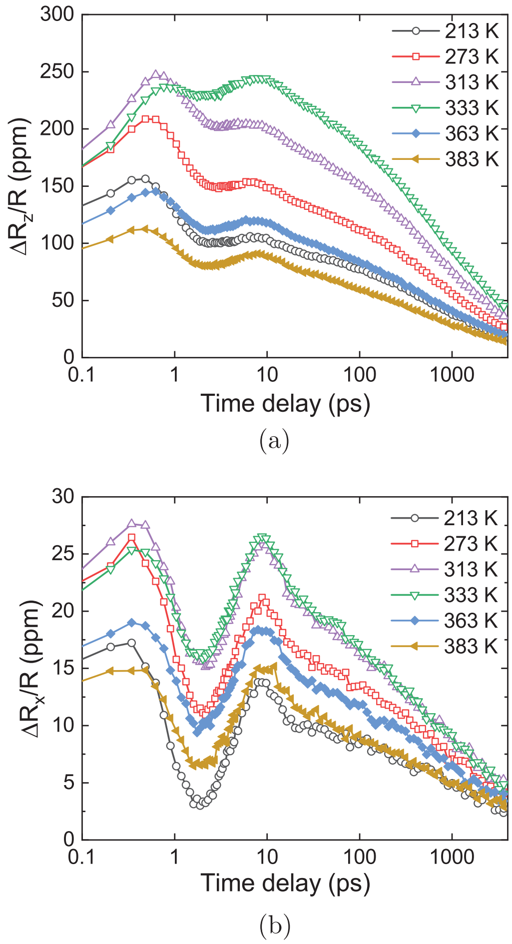

(a)

(b)

FIG. 5. Time-domain thermoreflectance (TDTR) data for the (010) face of Fe_2As with (a) probe polarization aligned along the z axis and (b) probe polarization aligned along the x axis. TDTR data for $\Delta R_z/\Delta T$ shown in panel (a) is approximately an order of magnitude larger than TDTR data for $\Delta R_x/\Delta T$ shown in panel (b). The temperature in the legend is the temperature of the sample stage; the spatially averaged temperature of the area of the sample that is measured in the TDTR experiment is the sum of stage temperature and the steady-state heating of 13 K. Empty symbols denote data for temperatures $T < T_N$; filled symbols are for data acquired at $T > T_N$.

reflection coefficients for light polarized along the z and x directions, respectively. $r_i = (n_i - 1)/(n_i + 1)$ with $n_i^2 = \varepsilon_{ii}$; ε_{ii} are the diagonal elements of the dielectric tensor.

The birefringence of Fe_2As is relatively small. We therefore define average quantities $\bar{n} = (n_x + n_z)/2$, $\bar{\varepsilon} = \bar{n}^2$, and $\bar{r} = (\bar{n} - 1)/(\bar{n} + 1)$. The complex rotation of the polarization of the reflected probe light is then

$$\Theta \approx \frac{(r_x - r_z)}{2\bar{r}} \approx \frac{(n_z - n_x)}{(1 - \bar{n}^2)} \approx \frac{(\varepsilon_{zz} - \varepsilon_{xx})}{2\sqrt{\bar{\varepsilon}}(1 - \bar{\varepsilon})}. \tag{1}$$

We use Eq. (1) to relate the polarization rotation angle to differences in the index of refraction or differences in the dielectric function. We evaluate Eq. (1) by using the measured refractive index $n = 2.9 + i3.3$. The real and imaginary parts of the TDTB signal can then be written as $\Delta\theta = 0.005(\Delta\varepsilon'_{zz} - \Delta\varepsilon'_{xx}) - 0.003(\Delta\varepsilon''_{zz} - \Delta\varepsilon''_{xx})$ and $\Delta\kappa = 0.003(\Delta\varepsilon'_{zz} - \Delta\varepsilon'_{xx}) + 0.005(\Delta\varepsilon''_{zz} - \Delta\varepsilon''_{xx})$, where ε'_{ii} and ε''_{ii} are the real and imaginary parts of the relative dielectric tensor.

Because the reflectance R_i is a function of the complex dielectric function ε_{ii}, the TDTR signal can be expanded as $\Delta R = \frac{\partial R}{\partial \varepsilon'}\Delta\varepsilon' + \frac{\partial R}{\partial \varepsilon''}\Delta\varepsilon''$. After taking partial derivative of reflectance and inserting the dielectric function calculated from the measured refractive index, the transient reflectance can be written as a linear combination of transient dielectric functions, $\Delta R_i = -0.01\Delta\varepsilon'_{ii} + 0.007\Delta\varepsilon''_{ii}$.

We note that the difference in the TDTR measurements along x and z closely resembles the real part of the TDTB signal, $\Delta\theta$. This is because the linear coefficients of the transient changes in the elements of the dielectric tensor that contribute to $\Delta R_x - \Delta R_z$ are approximately twice the linear coefficients of the transient changes in the elements of the dielectric tensor that contribute to $\Delta\theta$. In other words, $\Delta\theta \approx -(\Delta R_z - \Delta R_x)/2$. Alternatively, if we write the complex TDTB signal as an amplitude and phase in the form $\Delta\Theta = |z|e^{i\delta}$, the real part of the TDTB signal is $\Delta\theta = |z|\cos\delta$, while in TDTR measurement, $\Delta R_z - \Delta R_x = 2|z|$.

The per pulse heating, i.e., the temperature excursion produced by a single optical pulse of the pump beam, is $\Delta T \approx 3$ K. Due to the small temperature excursion, the change in the sublattice magnetization ΔM is small compared with the sublattice magnetization M, except for T very close to T_N. This justifies a description of the experiment in terms of linear response, except for T very close to T_N.

Since the (010) face of a tetragonal crystal is fundamentally anisotropic, we cannot directly interpret the signals plotted in Fig. 4 as the result of changes in magnetization with temperature. However, two aspects of the data suggest a prominent role of magnetism and magneto-optic effects. First, the real part of the TDTB signal [see Fig. 4(a)], and the TDTR signal measured with the probe polarization along the z axis [see Fig. 5(a)], show a significantly slower response when the sample temperature is close to the Néel temperature T_N. The transfer of thermal energy in a magnetic material is often described by a three-temperature model, in which energy is transferred between electrons, phonons, and magnons on ultrafast timescales [6,38]. Since the magnon contribution to heat capacity reaches a maximum at T_N, the temperature rise of the magnon system in response to heating of the electronic system by the pump optical pulse is expected to be slower at temperatures near T_N. We attribute the slower response at $T \approx T_N$ to this effect and conclude that the real part of the TDTB signal, and the TDTR signal measured with polarization along the z axis, are dominated by changes in the magnon temperature. The slowing down of the demagnetization of antiferromagnetic Fe_2As at $T \approx T_N$ is reminiscent of the slowing down of the demagnetization of ferromagnetic FePt:Cu at $T \approx T_C$ where T_C is the Curie temperature [38].

Second, the temperature dependence of the transient TDTB and TDTR signals at fixed time delays closely follows the magnetic heat capacity. In Fig. 6, we compare the complex thermo-birefringence signals $\Delta\Theta/\Delta T$ for the (010) plane of Fe_2As and the magnetic heat capacity derived from $C_m = C_{\text{tot}} - C_{\text{ph}} - C_e$. ($C_{\text{tot}}$ is measured by experiment and C_{ph} and C_e are calculated by DFT.) We use TDTB data acquired at pump-probe delay times near 100 ps when the electrons,

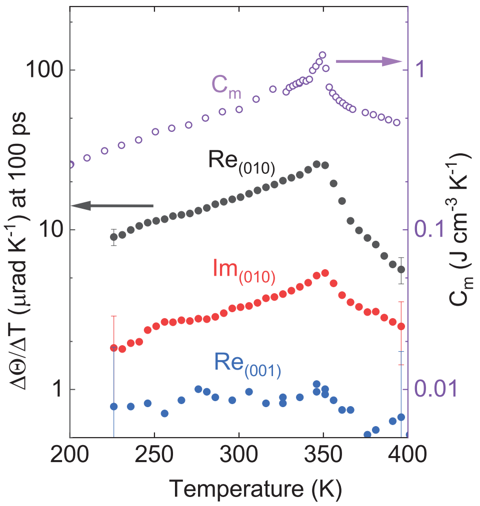

FIG. 6. Comparison between $\Delta\Theta/\Delta T$ and magnetic specific heat as a function of sample temperature. The values for $\Delta\Theta$ are for 100 ps delay time. For each sample temperature T, ΔT at 100 ps at is calculated from a thermal model that uses the measured total heat capacity and thermal conductivity of Fe_2As as inputs to the model. The sample temperature T includes the effects of steady-state heating of measurement area that is created by the absorbed laser power. The real and imaginary parts $\Delta\Theta/\Delta T$ measured for the (010) face have a similar temperature dependence as the magnetic specific heat C_m.

magnons, and phonons are in thermal equilibrium, and the strain and temperature gradients within an optical absorption depth of the surface are small. As we discuss in more detail below, we expect that for a single mechanism, the magnetic contribution to the dielectric function of an antiferromagnetic material will scale with the magnetic energy and, therefore, transient changes in the dielectric function produced by a small temperature excursion will scale with the magnetic heat capacity C_m. At $T \approx T_N$, we expect that $\Delta\Theta/\Delta T$ will be more smoothly varying with T than C_m because of the inhomogeneous temperature distribution across the lateral extent of the pump and probe beams in the experiment.

In Fig. 6 we also include data for the temperature dependence of $\Delta\theta$ measured on the crystallographically isotropic (001) plane. We consistently observe a small signal that is approximately independent of position. We believe there are two mechanisms that contribute to this null result. For the (001) plane of Fe_2As, the two degenerate domain orientations should produce a cancellation of any TDTB signal when measured on a length scale large compared with the characteristic domain size. We have not yet determined the domain structure of our Fe_2As crystals but evidence from related materials [39,40] suggest that the domain size is typically in the submicron range while the $1/e^2$ radius of the pump and probe laser beams is ≈ 5.5 μm. Furthermore, the lack of a significant TDTR signal for light polarized along the x direction of the (010) face suggests that magnetic contributions to the ε_{xx} and ε_{yy} elements of the dielectric tensor are small. We tentatively attribute the small transient birefringence signal that we observe on the (001) face to a small, uncontrolled miscut of the sample, i.e., a small misorientation between the surface normal and the c axis of the crystal.

Since both the real $\Delta\theta$ and imaginary $\Delta\kappa$ parts of the TDTB signals measured on the (010) face have a temperature dependence that resembles the magnetic heat capacity, we conclude that both $\Delta\theta$ and $\Delta\kappa$ have significant magnetic contributions. However, $\Delta\theta$ and $\Delta\kappa$ do not have the same dynamics; see Fig. 4. In the $\Delta\theta$ data set, with the exception of data collected at $T \approx T_N$, the signal reaches a peak response at short delay times on the order of 1 ps. We interpret this signal as arising from the same type of out-of-equilibrium ultrafast demagnetization that is typically observed for ferromagnetic materials using pump-probe measurements of first-order magneto-optic Kerr effects. However, we cannot yet reliably distinguish between magnetic, electronic, lattice temperature, and lattice strain contributions to $\Delta\theta$ or $\Delta\kappa$.

In the $\Delta\kappa$ data set, the signal reaches a peak response on a timescale on the order of 10 ps. We interpret this timescale as characteristic of the time needed to fully relax the thermoelastic stress within the near surface region of the crystal that determines the reflection coefficients of the probe beam. This interpretation is supported by the character of the TDTR signal measured on the (001) face; see Fig. 6, that also includes a large variation in the signal at $t < 20$ ps.

In most studies of the optical properties of materials, the thermal expansion of the material contributes to the temperature dependence of the dielectric tensor. Our experiments take place in a different regime. Thermal stress is generated when the pump optical pulse is partially absorbed by the near-surface region of the sample. Thermal strain in the in-plane direction is strongly suppressed in a pump-probe experiment because the thermal penetration depth, i.e., the depth of the heated region, is small compared with the lateral extent of the laser spot.

On the other hand, strain in the out-of-plane direction can contribute to TDTB and TDTR signals. The probe beam is sensitive to the dielectric tensor of the near-surface layer of the crystal that lies within an optical absorption depth of the surface. On this length scale, strain normal to the surface evolves on a timescale given by the optical absorption depth divided by the longitudinal speed of sound. The longitudinal speed of sound from our DFT calculations is ≈ 5 nm/ps. Therefore, the characteristic timescale is ≈ 4 ps. At $t \ll 4$ ps, *strain* normal to the surface is negligible; at $t \gg 4$ ps, *stress* normal to the surface is negligible. On long timescales, the decay of the strain normal to the surfaces will follow the decay of the surface temperature as heat diffuses into the bulk of the sample.

III. DISCUSSION

TDTB and TDTR signals are linearly related to transient changes in the dielectric function; see Eq. (1). The dielectric function tensor of magnetic materials can be written as [41]

$$\varepsilon_{ij} = \varepsilon_{ij}^{0} + K_{ijk}M_k + G_{ijkl}^{\mathrm{MM}}M_kM_l + G_{ijkl}^{\mathrm{ML}}M_kL_l + G_{ijkl}^{\mathrm{LL}}L_kL_l, \tag{2}$$

where the first term is the nonmagnetic contribution to ε_{ij}, K_{ijk} are the first-order magneto-optic coefficients, and G_{ijkl} are the second-order magneto-optic coefficients. M is net magnetization, and L is the Néel vector. Because the net magnetization is zero in a collinear AF, the linear term, M_kM_l term, and M_kL_l term can be neglected here, and we will use G_{ijkl} to represent G^{LL}_{ijkl} in what follows. We assume an equal population of magnetic domains with Néel vectors in the x and y directions.

To simplify the notation in the discussion below, we adopt the Voigt notation with, for example, G_{11}, G_{12}, and G_{31} replacing G_{1111}, G_{1122}, and G_{3311}, respectively. The tetragonal point-group symmetry of $\mathrm{Fe_2As}$ has six independent and nonzero elements of the second-order magneto-optic tensor: $G_{11} = G_{22}$, $G_{12} = G_{21}$, $G_{13} = G_{23} = G_{31} = G_{32}$, G_{33}, $G_{44} = G_{55}$, and G_{66}. We assume that there is no correlation in the sublattice magnetization along the z axis; therefore, terms that involve the z component of magnetization are small and we do not need to consider G_{33} or G_{44}. With the Néel vectors constrained to the x and y directions, the dielectric tensor is diagonal in the coordinate system of the crystal axes and we can also neglect G_{66}. The remaining contributions to the dielectric tensor involve three elements of the magneto-optic tensor:

$$\begin{aligned} \varepsilon_{11} &= G_{11}L_1^2 + G_{12}L_2^2 + \varepsilon_{11}^0, \\ \varepsilon_{22} &= G_{11}L_2^2 + G_{12}L_1^2 + \varepsilon_{22}^0, \\ \varepsilon_{33} &= G_{31}\left(L_1^2 + L_2^2\right) + \varepsilon_{33}^0. \end{aligned} \tag{3}$$

The microscopic mechanisms that contribute to the second-order magneto-optic coefficients G_{ijkl} include exchange interactions, spin-orbit coupling, and magnetostriction [16]. (Magnetostriction can be further divided into changes in the lattice parameters and, if the symmetry of the lattice is low enough, changes of the atomic positions within a unit cell [42].) Exchange interactions are usually assumed to dominate the isotropic contributions to the elements of G_{ijkl}, i.e., magnetic contributions that are independent of the orientation of the Néel vector. (The term "isotropic" does not imply that the magnetic contributions are the same for all elements of the dielectric tensor.) Spin-orbit interactions are usually assumed to dominate anisotropic contributions to G_{ijkl}, i.e., contributions that depend on the orientation of the Néel vector. Isotropic contributions are larger than anisotropic contributions in most materials [16,43]. In collinear AFs with cubic symmetry, the anisotropic contribution to the dielectric function can be isolated from the isotropic contribution because birefringence can only be generated by anisotropic terms [16,17].

Within the easy-plane of AFs with cubic, tetragonal, or hexagonal symmetry, optical birefringence can sometimes be used to image magnetic domains [44] because the anisotropy of the dielectric tensor is coupled to the orientation of the Néel vector. In a recent study of tetragonal CuMnAs [18], the transient birefringence signal measured in the x-y plane demonstrated the potential of using the anisotropic Voigt effect for determining the magnetic domain structure of tetragonal AFs. We find, however, that the Voigt effect is small for $\mathrm{Fe_2As}$ at the wavelength of our laser, $\lambda = 783$ nm, and we have not yet been able to use TDTB signals to study the magnetic domain structure.

On the (010) face of $\mathrm{Fe_2As}$, approximately one half of the domains have Néel vectors in the in-plane x direction and the other half of the domains have Néel vectors in the out-of-plane y direction. TDTB signals acquired on the (010) plane are, in principle, sensitive to contributions from anisotropic terms in the magneto-optic coefficients generated by domains with Néel vectors in the x direction. TDTB signals are sensitive to contributions from isotropic terms generated by domains with Néel vectors in both the x and y directions. If the anisotropic contributions, e.g., the Voigt effect, were dominant, then $G_{11} \gg G_{31}$ [23,45]. However, the TDTR data, see Fig. 5, lead us to conclude that $\Delta\varepsilon_{zz} \gg \Delta\varepsilon_{xx}$, $G_{11} \ll G_{31}$, and the isotropic contribution to ε_{zz} is the dominant effect.

In previous studies of tetragonal transition-metal fluorides [16,46], the derivative of the magnetic linear birefringence with respect to temperature $d(\Delta n_m)/dT$, where Δn_m is the difference in the index of refraction between z and x axes of the crystal, has been shown to have the same temperature dependence as the magnetic specific heat. This behavior is expected because both the magnetic contributions to the dielectric function and the magnetic energy include terms that involve correlations of the products of the spin angular moment at different lattice sites. Contributions to the magneto-optic coefficients from various terms in the Hamiltonian could, however, have different constants of proportionality. Furthermore, in our time-domain thermo-birefringence (TDTB) measurements of the (010) face of the $\mathrm{Fe_2As}$ crystal, there are nonmagnetic contributions to the TDTB signals that come from thermal excitations of electrons and phonons. The fact that the TDTB signals closely resemble the temperature dependence of the magnetic heat capacity supports our conclusion that the TDTB signals are dominated by a magnetic contribution with a single underlying mechanism.

If we assume that the magnetic contribution dominates the temperature-dependence of ε_{33}, the magneto-optic coefficient G_{31} can be estimated by using the value of $\Delta\varepsilon_{33}$ and $\Delta(M_A^2)$, where M_A is sublattice magnetization of the AF. We estimate $\Delta(M_A^2)$ from our magnetic heat-capacity data as described in the Supplemental Material [34]. Because the sublattice magnetization is always real, the magneto-optic coefficient G_{31} is complex since $\Delta\varepsilon_{33}$ is a complex number.

$$G_{31} = \frac{\Delta\varepsilon_{33}/\Delta T}{2\Delta\left(M_A^2\right)/\Delta T} = \frac{\left(\Delta\varepsilon_{33}' + i\Delta\varepsilon_{33}''\right)}{2\Delta\left(M_A^2\right)}. \tag{4}$$

Inserting the value of the transient dielectric function and the temperature excursion of 1.5 K at a delay time of 100 ps and ambient temperature of 293 K, we find $G_{31} = (0.85 - i0.12) \times 10^{-12}\ \mathrm{A^{-2}\,m^2}$. We emphasize that this value for G_{31} should be considered an estimate because we have assumed that the magnetic contribution dominates the temperature dependence of ε_{33}.

Finally, we compare the magnitude of our result for G_{31} of $\mathrm{Fe_2As}$ with the quadratic magneto-optic coefficients of several more commonly studied magnetic materials, see Table I. In Table I, G tensors are G^{MM} for ferromagnets and G^{LL} for antiferromagnets. In studies of ferromagnetic materials (Fe, Co, Ni, and $\mathrm{Y_3Fe_5O_{12}}$), the magnetization vector can be manipulated by an external field and therefore the elements of the quadratic magneto-optic tensor G_{ij} can be calculated by using Eq. (3) and $M^2 = M_s^2$, where M_s is the

TABLE I. Comparison of the quadratic magneto-optic coefficient G_{31} of antiferromagnetic Fe_2As determined in our work with selected previous studies of ferromagnetic (Fe, Co, Ni, $Y_3Fe_5O_{12}$) and antiferromagnetic (MnF_2, CoF_2) materials. Ni and Fe_2As have relatively large quadratic magneto-optic coefficients.

Materials	Wavelength (nm)	Magneto-optic data	Magnetization	Quadratic magneto-optic coefficient ($10^{-14}\mathrm{A}^{-2}\,\mathrm{m}^2$)
Fe [47]	670	$\varepsilon_{11}-\varepsilon_{12}=-(5.0+i3.5)\times10^{-2}$	$1.8\times10^{6}\,\mathrm{A\,m^{-1}}$	$G_{11}-G_{12}=-1.5-i1.1$
Fe [48]	670	$\varepsilon_{11}-\varepsilon_{12}=-0.15+i0.07$	$1.8\times10^{6}\,\mathrm{A\,m^{-1}}$	$G_{11}-G_{12}=-4.6+i2.1$
Co [48]	670	$\varepsilon_{11}-\varepsilon_{12}=0.10-i0.13$	$1.4\times10^{6}\,\mathrm{A\,m^{-1}}$	$G_{11}-G_{12}=5.1-i6.6$
Ni [48]	670	$\varepsilon_{11}-\varepsilon_{12}=-0.75+i0.20$	$5.0\times10^{5}\,\mathrm{A\,m^{-1}}$	$G_{11}-G_{12}=(-300+i80)$
$Y_3Fe_5O_{12}$ [49]	1150	$\lvert n_\perp-n_\parallel\rvert=3.9\times10^{-6}$	$1.4\times10^{5}\,\mathrm{A\,m^{-1}}$	$G_{11}-G_{12}=1.6$
$KNiF_3$ [17]	632.8	$n_m=3.3\times10^{-3}$	$1.3\times10^{5}\,\mathrm{A\,m^{-1}}$	$G_{11}=60$
MnF_2 [50]	632.8	$d(\Delta n_m)/dT=5.0\times10^{-5}\mathrm{K^{-1}}$	$d(M^2)/dT$ $=-1.3\times10^{10}\mathrm{A^2\,m^{-2}\,K^{-1}}$	$\lvert G_{13}\rvert=1.2$
CoF_2 [50]	632.8	$d(\Delta n_m)/dT=2.5\times10^{-5}\mathrm{K^{-1}}$	$d(M^2)/dT$ $=-1.2\times10^{10}\mathrm{A^2\,m^{-2}\,K^{-1}}$	$\lvert G_{33}-G_{13}\rvert=0.63$
Fe_2As	783	$d(\varepsilon_{33})/dT$ $=(-1.5+i0.21)\times10^{-3}\mathrm{K^{-1}}$	$d(M^2)/dT$ $=-8.8\times10^{8}\mathrm{A^2\,m^{-2}\,K^{-1}}$	$G_{31}=(85-i12)$

saturation magnetization. In studies of antiferromagnetic materials (MnF_2, CoF_2, and Fe_2As), typically, the Néel vector cannot be controlled with an external field and the values of G_{ij} are more difficult to determine. The measurements of antiferromagnetic MnF_2 and CoF_2 reported in Ref. [50] are collected from a crystallographic anisotropic plane; therefore, the magnetic birefringence data that we use in this analysis are the temperature derivatives of the birefringence data with the additional assumption that the magnetic birefringence has a stronger dependence on temperature than the crystalline birefringence. We used $M^2 = M_A^2$ to calculate the G_{ij} tensor for antiferromagnets, where M_A is sublattice magnetization. Typically, G_{11} and G_{13} or G_{12} cannot be determined separately based on birefringence data alone. Compared with the other materials listed in Table I, Fe_2As and Ni have relatively large quadratic magneto-optic coefficients.

IV. CONCLUSION

In collinear antiferromagnetic materials, the contribution to the diagonal elements of the dielectric tensor that are quadratic in sublattice magnetization can be probed with transient birefringence or reflectance measurements. In our measurement of time-domain thermo-birefringence (TDTB) and thermo-reflectance (TDTR) of Fe_2As, we observe that the dominant response of the dielectric tensor is in the z direction and perpendicular to the Néel vector. The temperature dependences of the TDTB signals closely follow the temperature dependence of the magnetic heat capacity, as expected if the exchange interaction is the dominant magnetic contribution to the dielectric function. In comparison with other magnetic materials, Fe_2As has relatively large quadratic magneto-optic coefficient at 783 nm.

ACKNOWLEDGMENTS

This work was undertaken as part of the Illinois Materials Research Science and Engineering Center, supported by the National Science Foundation MRSEC program under NSF Award No. DMR-1720633. This work made use of the Illinois Campus Cluster, a computing resource that is operated by the Illinois Campus Cluster Program (ICCP) in conjunction with the National Center for Supercomputing Applications (NCSA) and which is supported by funds from the University of Illinois at Urbana-Champaign. This research is part of the Blue Waters sustained-petascale computing project, which is supported by the National Science Foundation (Awards No. OCI-0725070 and No. ACI-1238993) and the state of Illinois. Blue Waters is a joint effort of the University of Illinois at Urbana-Champaign and its National Center for Supercomputing Applications. This research used resources of the Spallation Neutron Source, a DOE Office of Science User Facility operated by Oak Ridge National Laboratory, and the Advanced Photon Source, a DOE Office of Science User Facility operated for the DOE Office of Science by Argonne National Laboratory under Contract No. DE-AC02-06CH11357. Z.D. acknowledges support from the Swedish Research Council (VR) under Grant No. 2015-00585, co-funded by Marie Skłodowska-Curie Actions (Project INCA 600398).

---

[1] R. Duine, Spintronics: An alternating alternative, Nat. Mater. **10**, 344 (2011).

[2] J. Sinova and I. Žutić, New moves of the spintronics tango, Nat. Mater. **11**, 368 (2012).

[3] T. Satoh, B. B. Van Aken, N. P. Duong, T. Lottermoser, and M. Fiebig, Ultrafast spin and lattice dynamics in antiferromagnetic Cr_2O_3, Phys. Rev. B **75**, 155406 (2007).

[4] C. Tzschaschel, K. Otani, R. Iida, T. Shimura, H. Ueda, S. Günther, M. Fiebig, and T. Satoh, Ultrafast optical excitation of coherent magnons in antiferromagnetic NiO, Phys. Rev. B **95**, 174407 (2017).

[5] A. M. Kalashnikova, A. V. Kimel, and R. V. Pisarev, Ultrafast opto-magnetism, Phys. Usp. **58**, 969 (2015).

[6] E. Beaurepaire, J.-C. Merle, A. Daunois, and J.-Y. Bigot, Ultrafast Spin Dynamics in Ferromagnetic Nickel, Phys. Rev. Lett. **76**, 4250 (1996).

[7] S. Visnovsky, V. Prosser, R. Krishnan, V. Parizek, K. Nitsch, and L. Svobodova, Magnetooptical polar Kerr effect in ferrimagnetic garnets and spinels, IEEE Trans. Magn. **17**, 3205 (1981).

[8] J. McCord, Progress in magnetic domain observation by advanced magneto-optical microscopy, J. Phys. D: Appl. Phys. **48**, 333001 (2015).

[9] D. S. Schmool, N. Keller, M. Guyot, R. Krishnan, and M. Tessier, Magnetic and magneto-optic properties of orthoferrite thin films grown by pulsed-laser deposition, J. Appl. Phys. **86**, 5712 (1999).

[10] T. Higo, H. Man, D. B. Gopman, L. Wu, T. Koretsune, O. M. van 't Erve, Y. P. Kabanov, D. Rees, Y. Li, M.-T. Suzuki *et al.*, Large magneto-optical Kerr effect and imaging of magnetic octupole domains in an antiferromagnetic metal, Nat. Photonics **12**, 73 (2018).

[11] P. Nemec, M. Fiebig, T. Kampfrath, and A. V. Kimel, Antiferromagnetic opto-spintronics, Nat. Phys. **14**, 229 (2018).

[12] W. Muir and J. O. Ström-Olsen, Electrical resistance of single-crystal single-domain chromium from 77 to 325 K, Phys. Rev. B **4**, 988 (1971).

[13] T. Jungwirth, X. Marti, P. Wadley, and J. Wunderlich, Antiferromagnetic spintronics, Nat. Nanotechnol. **11**, 231 (2016).

[14] S. Y. Bodnar, L. Šmejkal, I. Turek, T. Jungwirth, O. Gomonay, J. Sinova, A. Sapozhnik, H.-J. Elmers, M. Kläui, and M. Jourdan, Writing and reading antiferromagnetic Mn_2Au by Néel spin-orbit torques and large anisotropic magnetoresistance, Nat. Commun. **9**, 348 (2018).

[15] S. S. Dhesi, G. van der Laan, and E. Dudzik, Determining element-specific magnetocrystalline anisotropies using x-ray magnetic linear dichroism, Appl. Phys. Lett. **80**, 1613 (2002).

[16] J. Ferré and G. A. Gehring, Linear optical birefringence of magnetic crystals, Rep. Prog. Phys. **47**, 513 (1984).

[17] P. A. Markovin, R. V. Pisarev, G. A. Smolensky, and P. P. Syrnikov, Observation of isotropic magnetic contribution to the refractive index of ABF_3-type cubic crystals, Solid State Commun. **19**, 185 (1976).

[18] V. Saidl, P. Němec, P. Wadley, V. Hills, R. P. Campion, V. Novák, K. W. Edmonds, F. Maccherozzi, S. S. Dhesi, B. L. Gallagher *et al.*, Optical determination of the Néel vector in a CuMnAs thin-film antiferromagnet, Nat. Photonics **11**, 91 (2017).

[19] H. Katsuraki and N. Achiwa, The magnetic structure of Fe_2As, J. Phys. Soc. Jpn. **21**, 2238 (1966).

[20] N. Achiwa, S. Yano, M. Yuzuri, and H. Takaki, Magnetic anisotropy in the c-plane of Fe_2As, J. Phys. Soc. Jpn. **22**, 156 (1967).

[21] J. M. Perez-Mato, S. V. Gallego, E. S. Tasci, L. Elcoro, G. de la Flor, and M. I. Aroyo, Symmetry-based computational tools for magnetic crystallography, Annu. Rev. Mater. Res. **45**, 217 (2015).

[22] L. M. Corliss, J. M. Hastings, W. Kunnmann, R. J. Begum, M. F. Collins, E. Gurewitz, and D. Mukamel, Magnetic phase diagram and critical behavior of Fe_2As, Phys. Rev. B **25**, 245 (1982).

[23] H. Le Gall, T. K. Vien, and B. Desormiere, Theory of the elastic and inelastic scattering of light by magnetic crystals. II. Second-order processes, Phys. Status Solidi B **47**, 591 (1971).

[24] K. Kang, Y. K. Koh, C. Chiritescu, X. Zheng, and D. G. Cahill, Two-tint pump-probe measurements using a femtosecond laser oscillator and sharp-edged optical filters, Rev. Sci. Instrum. **79**, 114901 (2008).

[25] J. Kimling, A. Philippi-Kobs, J. Jacobsohn, H. P. Oepen, and D. G. Cahill, Thermal conductance of interfaces with amorphous SiO_2 measured by time-resolved magneto-optic Kerr-effect thermometry, Phys. Rev. B **95**, 184305 (2017).

[26] G. Kresse and J. Furthmüller, Efficient iterative schemes for *ab initio* total-energy calculations using a plane-wave basis set, Phys. Rev. B **54**, 11169 (1996).

[27] G. Kresse and D. Joubert, From ultrasoft pseudopotentials to the projector augmented-wave method, Phys. Rev. B **59**, 1758 (1999).

[28] M. Gajdoš, K. Hummer, G. Kresse, J. Furthmüller, and F. Bechstedt, Linear optical properties in the projector-augmented wave methodology, Phys. Rev. B **73**, 045112 (2006).

[29] J. P. Perdew, K. Burke, and M. Ernzerhof, Generalized Gradient Approximation Made Simple, Phys. Rev. Lett. **77**, 3865 (1996).

[30] P. E. Blöchl, Projector augmented-wave method, Phys. Rev. B **50**, 17953 (1994).

[31] H. J. Monkhorst and J. D. Pack, Special points for Brillouin-zone integrations, Phys. Rev. B **13**, 5188 (1976).

[32] A. Togo and I. Tanaka, First principles phonon calculations in materials science, Scr. Mater. **108**, 1 (2015).

[33] D. A. Zocco, D. Y. Tütün, J. J. Hamlin, J. R. Jeffries, S. T. Weir, Y. K. Vohra, and M. B. Maple, High pressure transport studies of the LiFeAs analogs $CuFeTe_2$ and Fe_2As, Supercond. Sci. Technol. **25**, 084018 (2012).

[34] See Supplemental Material at http://link.aps.org/supplemental/10.1103/PhysRevMaterials.3.124408 for Stochiometry of Fe_2As sample.

[35] N. D. Mermin, Thermal properties of the inhomogeneous electron gas, Phys. Rev. **137**, A1441 (1965).

[36] D. G. Cahill, Analysis of heat flow in layered structures for time-domain thermoreflectance, Rev. Sci. Instrum. **75**, 5119 (2004).

[37] D. Bossini, A. M. Kalashnikova, R. V. Pisarev, T. Rasing, and A. V. Kimel, Controlling coherent and incoherent spin dynamics by steering the photoinduced energy flow, Phys. Rev. B **89**, 060405(R) (2014).

[38] Johannes Kimling, Judith Kimling, R. B. Wilson, B. Hebler, M. Albrecht, and D. G. Cahill, Ultrafast demagnetization of FePt:Cu thin films and the role of magnetic heat capacity, Phys. Rev. B **90**, 224408 (2014).

[39] M. J. Grzybowski, P. Wadley, K. W. Edmonds, R. Beardsley, V. Hills, R. Campion, B. L. Gallagher, J. S. Chauhan, V. Novak, T. Jungwirth, F. Maccherozzi, and S. S. Dhesi, Imaging Current-Induced Switching of Antiferromagnetic Domains in CuMnAs, Phys. Rev. Lett. **118**, 057701 (2017).

[40] A. A. Sapozhnik, M. Filianina, S. Yu. Bodnar, A. Lamirand, M.-A. Mawass, Y. Skourski, H.-J. Elmers, H. Zabel, M. Kläui, and M. Jourdan, Direct imaging of antiferromagnetic domains in Mn_2Au manipulated by high magnetic fields, Phys. Rev. B **97**, 134429 (2018).

[41] V. V. Eremenko, N. Kharchenko, Y. G. Litvinenko, and V. M. Naumenko, *Magneto-Optics and Spectroscopy of Antiferromagnets* (Springer Science & Business Media, 2012).

[42] W. Jauch, Structural origin of magnetic birefringence in rutile-type antiferromagnets, Phys. Rev. B **44**, 6864 (1991).

[43] S. Borovik-Romanov, N. M. Kreines, A. A. Pankov, and M. A. Talalayev, Magnetic birefringence of light in antiferromagnetic transition-metal fluorides, Sov. Phys.-JETP **37**, 890 (1973).

[44] N. B. Weber, C. Bethke, and F. U. Hillebrecht, Imaging of antiferromagnetic domains at the NiO(100) surface by linear dichroism in near UV photoemission microscopy, J. Magn. Magn. Mater. **226**, 1573 (2001).

[45] N. Tesařová, P. Němec, E. Rozkotová, J. Šubrt, H. Reichlová, D. Butkovičová, F. Trojánek, P. Malý, V. Novák, and T. Jungwirth, Direct measurement of the three-dimensional magnetization vector trajectory in gammas by a magneto-optical pump-and-probe method, Appl. Phys. Lett. **100**, 102403 (2012).

[46] I. Jahn and H. Dachs, Change of the optical birefringence associated with the antiferromagnetic ordering of MnF_2, FeF_2, CoF_2, and NiF_2, Solid State Commun. **9**, 1617 (1971).

[47] J. H. Liang, X. Xiao, J. X. Li, B. Zhu, J. Zhu, H. Bao, L. Zhou, and Y. Z. Wu, Quantitative study of the quadratic magneto-optical Kerr effects in Fe films, Opt. Express **23**, 11357 (2015).

[48] J. Hamrlová, D. Legut, M. Veis, J. Pištora, and J. Hamrle, Principal spectra describing magnetooptic permittivity tensor in cubic crystals, J. Magn. Magn. Mater. **420**, 143 (2016).

[49] R. V. Pisarev, I. G. Sinii, N. N. Kolpakova, and Y. M. Yakovlev, Magnetic birefringence of light in iron garnets, Sov. Phys. JETP **33**, 1175 (1971).

[50] I. R. Jahn, Linear magnetic birefringence in the antiferromagnetic iron group difluorides, Phys. Status Solidi B **57**, 681 (1973).